J. Mech. Phys. Solids 152 (2021) 104421

Contents lists available at ScienceDirect

Journal of the Mechanics and Physics of Solids

journal homepage: www.elsevier.com/locate/jmps

Role of interface-affected dislocation motion on the strength of Mg/Nb nanolayered composites inferred by dual-mode confined layer slip crystal plasticity

Jiaxiang Wang [a,*], Marko Knezevic [b], Manish Jain [c,d], Siddhartha Pathak [c,e], Irene J. Beyerlein [a,f]

[a] Department of Mechanical Engineering, University of California, Santa Barbara, CA 93106-5070, United States
[b] Department of Mechanical Engineering, University of New Hampshire, Durham, NH 03824, United States
[c] Department of Chemical and Materials Engineering, University of Nevada, Reno, NV 89557, United States
[d] EMPA, Swiss Federal Laboratory for Materials Science and Technology, Feuerwerkerstrasse 39, Thun 3602, Switzerland
[e] Department of Materials Science and Engineering, Iowa State University, Ames, IA 50011, United States
[f] Materials Department, University of California, Santa Barbara, CA 93016-5050, United States

ARTICLE INFO

Keywords:
A. Dislocation
B. Layered material
B. Crystal Plasticity
C. Finite element
Interface

ABSTRACT

In this work, we present a nanostructure-sensitive crystal plasticity model for the deformation response of nanolaminate composites. The model is applied to investigate the strength of Mg/Nb nanocomposites, wherein the Mg phase has either a hexagonal close-packed (HCP) or a body-centered cubic (BCC) crystal structure. To account explicitly for the effects of layer thickness and biphase interface on crystallographic slip, the model features a hardening law, called dual-mode confined layer slip (CLS). The model is applied to a suite of stress-strain measurements made on Mg/Nb nanocomposites, varying layer thickness, texture, and interface structure. Experiments show that the BCC/BCC Mg/Nb nanocomposites achieve substantially higher strength than the HCP/BCC nanocomposites. Apart from the finer layer thicknesses, the model indicates that the pseudomorphic BCC Mg phase contributes to strength by increasing the slip strengths of the ⟨111⟩ slip modes compared to the ⟨a⟩ slip modes in HCP Mg. It also suggests that the coherent interface poses less resistance to dislocation motion than the incoherent interface. It is, therefore, found that the BCC/BCC composite strength benefited from both the confinement on dislocation motion imposed by the reduced layer thickness and higher inherent strength of its BCC phase, but that it would be even higher if the interface was not a sharp coherent interface.

1. Introduction

Over the years, metallic nanolayered composites (MNCs) have been drawing increasing attention in the materials community. MNCs are a type of composite made from constituents with different physical properties that are nanoscale in dimension. Multiple studies on MNCs have reported that compared with coarse-layered composites of the same composition (layer thickness $h \sim 10^{-3} \sim 10^{-5}$m), MNCs exhibit substantially better thermal stability, shock resistance, radiation resistance, and ultra-high strength (Cao et al., 2019; Chen et al., 2020a; Clemens et al., 1999; Han et al., 2011; Mara and Beyerlein, 2015; Mara et al., 2008; Misra et al.,

* Corresponding author.
E-mail address: jiaxiangwang@ucsb.edu (J. Wang).

https://doi.org/10.1016/j.jmps.2021.104421
Received 3 February 2021; Received in revised form 20 March 2021; Accepted 29 March 2021
Available online 1 April 2021

2005, 2004; Misra and Hoagland, 2005). Among these properties, the enhancements in strengths have been the most impressive, ranging from three to ten times that of the coarser layered version, inspiring many investigations to study their mechanistic or microstructural origins.

In MNCs, the relatively small h compared with the dislocation core ($\sim$ 1 nm) limits the amount of volume in which dislocations can be stored or pile up and how far dislocations can move (Chen et al., 2020b; Hoagland et al., 2004; Misra et al., 2005; Zhang et al., 2017; Zhao et al., 2019). Consequently, in this nano-scale limit, the dislocation processes involve one to a few dislocations. Fine nanoscale layers also limit the size of grain boundary sources and force dislocations to bow-out or thread through the layers between adjacent interfaces (Chen et al., 2020b; Mastorakos et al., 2009; Zbib et al., 2011). The latter has been conventionally referred to as confined layer slip (CLS), in which an individual dislocation must thread in between the two interfaces in order to glide on its plane. Due to the increased line tension as it bows within the layer, the dislocation critical resolved shear stress (CRSS) scales as $(ln(h)/h)$ (Anderson et al., 1999; Ardeljan et al., 2018; Chen et al., 2020b; Liu et al., 2019; Misra et al., 2005). This mechanism for dislocation glide indicates that MNC strength in the nanoscale regime should depend sensitively on the individual layer thickness h, increasing as h decreases.

Besides the fine nanoscale layering, the types of biphase interfaces, the crystal structure, and crystallographic orientations of the constituents can also affect the strength of MNCs. Certain types of interfaces are more thermally stable than others or provide more resistance (Beyerlein et al., 2015; Snel et al., 2017; Wang et al., 2018; Zhang et al., 2017). The introduction of high density, coherent interfaces or interfaces free of extrinsic defects, can result in higher material stability with respect to temperature, high rates, and large strain deformations (Mara and Beyerlein, 2015; Yang et al., 2019).

Another phenomenon that may accompany reductions in layer thickness in MNCs is a pseudo-morphic phase transformation (Frank and Vandermerwe, 1949; Jesser, 1969). When two metals of dissimilar crystal structure are joined, a phase transformation can be induced in one phase from the stable crystal structure to a new crystal structure that matches the adjoining phase and the biphase interface between them is coherent. For this to happen, the layer thickness of the transformed phase needs to be sufficiently fine such that the energetic preference of a low energy, coherent bimetal interface outweighs the energetic penalty associated with the coherency strains. As a result, one constituent adopts the crystal structure of the other.

One material that has benefitted from a pseudomorphic phase transformation is magnesium (Mg) (Ham and Zhang, 2011). The mechanical properties of Mg and its alloys have been extensively studied as these materials could have important applications where high strength and lightweight materials are desirable, such as military, aerospace, and portable electronics industries (Zeng et al., 2019). However, some limitations need to be overcome. The inherent strength of Mg at room temperature relative to other commonly available metals, like steel, is very low (Pan et al., 2016). Also, due to the low symmetry HCP crystal structure of Mg, its plastic behavior is sensitive to loading direction, temperature, and strain rate, leading to low room-temperature formability (Arul Kumar et al., 2017; Miller et al., 2016). By transforming from an HCP metal to a pseudomorphic body-centered cubic structure (BCC) metal, Mg changes its slip properties dramatically. Usually the critical stresses in Mg for pyramidal $\langle c + a \rangle$ slip are several times larger than those in the basal $\langle a \rangle$ slip (Bong et al., 2019; Risse et al., 2017). Thus the crystals in which the stress orientations benefit $\langle c + a \rangle$ slip activity deform under higher stress than those oriented well for $\langle a \rangle$ slip (Ardeljan et al., 2016; Kabirian et al., 2015; Kumar et al., 2017a, 2017b; Sandlöbes et al., 2011; Savage et al., 2020). Meanwhile, in BCC crystal, at least 48 available slip systems with similar activation stress and a more symmetric structure make it more ductile than HCP metals.

It has been shown that when combined with Nb in an MNC, the Mg phase can change from HCP to BCC (Ham and Zhang, 2011; Jain et al., 2019; Pathak et al., 2017). Based on DFT calculations and theory, a critical layer thickness for the transformation was predicted to be $h = 4.2$ nm (Kumar et al., 2014). TEM, X-ray diffraction, and synchrotron experiments have shown that $h = 5.5$ nm can produce an MNC with a uniformly BCC Mg phase. Recent work has reported that when compressed normal to the layers, the 5.5/5.5 nm BCC/BCC Mg/Nb composites were approximately 50% stronger than a 35/65 nm HCP/BCC Mg/Nb composite and sustained a higher strain to failure (Pathak et al., 2017). The role of the pseudomorphic phase in strengthening, however, remains to be clarified. Furthermore, these two composites differ in many ways apart from the HCP to BCC phase change. The interface type has also changed from an incoherent HCP/BCC to a coherent BCC/BCC interface, the crystallographic texture has been completely altered, and the layer thickness has reduced by an order of magnitude.

To simulate the deformation response of nanolaminates, a 3D model, accounting for the texture, interface character, and slip systems is needed. Mean-field polycrystal plasticity models have indeed become a commonly used approach to determine the constitutive response of polycrystalline materials (Al–Fadhalah et al., 2005; Lebensohn and Tomé, 1993; Nizolek et al., 2016; Wang et al., 2020). For many years, the spatially resolved crystal plasticity mechanics techniques, such as crystal plasticity finite element (CPFE), have been used to research the deformation behavior of polycrystalline materials (Bronkhorst et al., 1992; Hansen et al., 2013; Kalidindi et al., 1992, 2006; Knezevic and Beyerlein, 2018; Zhang et al., 2019). While computationally more intensive, unlike mean-field models, 3D full-field, crystal plasticity models, like CPFE, spatially resolve the topology and crystallinity of the local neighborhood of each grain, an important ability for the highly oriented and layered materials of interest here. In the CPFE method, the deformation at each point in the material is governed by elasticity and dislocation slip via crystal plasticity. In a deformation simulation, CPFE can relate the macroscopic stress-strain response, typically measured experimentally, with the underlying slip and twinning activity (Ardeljan and Knezevic, 2018; Ardeljan et al., 2018; Bronkhorst et al., 2006; Roters et al., 2010). Over the bulk material, it can predict the evolution in texture, grain boundary character, and interface character distributions during deformation. At the microstructural level, it can calculate the spatially resolved inter- and intra-granular stress, strain, and rotational fields in a 3D microstructure. Recently a 3D CPFE model was developed to calculate the elastic and plastic stress-strain responses of the Mg/Nb nanolaminates (Ardeljan et al., 2018). Comparisons with the elastic curves from micropillar testing enabled calculation of the elastic constants of BCC Mg, which were not possible earlier even with DFT or high-pressure synchrotron diffraction (Su et al., 2020). For the plastic response, the model incorporated the standard CLS law in order to account for the h-effect on strength (Misra et al., 2005).

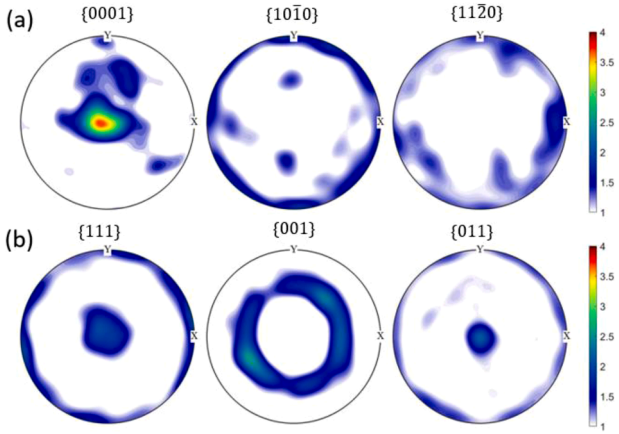

Fig. 1. Initial texture for the (a) Mg phase in the in the HCP Mg/BCC Nb nanocomposites. (b) The Nb phases and Mg phase in the BCC Mg/Nb nanocomposite had the same initial texture. The deposition direction is the Z direction and X-Y are the two in-plane directions.

While the *h*-size effect on the plastic responses of these composites was captured, it was still unclear which microstructural consequence of the pseudomorphic change was responsible for the high strength, since too few cases and loading directions were considered.

In this work, using 3D CPFE modeling, we investigate the strengthening mechanisms of pseudomorphic BCC Mg/Nb composites. We present a modified confined layer slip model, called dual-mode CLS, and incorporate it into a 3D crystal plasticity finite element model that explicitly represents the grain structure and texture of the nanocrystalline layer in order to calculate the deformation responses of the nanocomposites. The model is applied to a set of stress-strain measurements made on Mg/Nb nanocomposites. Most of the experimental data were previously reported; however, here we carry out just a few key distinct tests, such that the data set spans three types of MNCs, which differ not only in crystal structure for the Mg phase and nanolayer thicknesses, but also in interface type, texture, and loading direction. Taken together, we identify that the pseudomorphic BCC Mg phase is stronger than the HCP Mg phase, with the slip strengths of {110} and {112} <111> slip in BCC being higher than basal and prismatic <a> slip in HCP. The analysis indicates that coherent interface, however, is weaker than the incoherent one; therefore, the reduction in layer thickness was helpful for strengthening the material and compensating for the otherwise weakening effect of this change in interface type. Last, the model forecasts that if the Mg/Nb composite were to remain HCP/BCC with reductions in layer thickness, the size effect in strengthening would be minimal since Nb accommodates more of the deformation. As a pseudomorphic phase, Mg, on the other hand, accommodates more of the applied strain than Nb.

This paper is structured as follows. We begin with a description of the experimental synthesis and micropillar methods used, followed by a review of the CPFE formulation. Then the dual-mode CLS model for the hardening law for slip is presented. Next, the methods for building the 3D nanolaminate microstructures, their properties, and boundary conditions for CPFE deformation simulation are described. The results are then presented, beginning with direct comparison with stress-strain response in different loading directions and layer thickness and including discussion of the slip and interface strengths in the pseudomorphic BCC phase of Mg and relative activities of the slip modes, which are not available experimentally. We conclude with an analysis of the data to identify the key contributors for strengthening the BCC Mg/Nb nanolayer composite over the HCP Mg/Nb composite.

2. Materials and experimental methods

Mg/Nb MNCs were synthesized via PVD, using methods described in Ardeljan et al. (2018), Jain et al. (2019) and Pathak et al. (2017). Here we study a set of MNCs made with one of three layer thicknesses– 5.5/5.5 nm, 7/7 nm, and 35/65 nm Mg/Nb nanocomposites. Note that only the 7/7 nm nanocomposite is newly made here, and the others have been characterized previously.

X-ray diffraction (XRD) was used to measure the initial texture of each phase and transmission electron microscopy (TEM) was used to confirm the uniformity in layer thicknesses (Jain et al., 2021). Fig. 1 shows the initial texture of the HCP Mg phase and the BCC Mg and Nb phases from XRD Ardeljan et al. (2018). The Nb and Mg phases in the 5.5/5.5 nm composites are the same, wherein the {110} poles are aligned through the thickness of the film. In the HCP Mg phase, the basal poles are strongly aligned through the thickness. The finest 5.5 nm BCC Mg nanolaminates had nearly equal Mg and Nb layer thicknesses and, consistent with the XRD results, TEM confirmed that the Mg phase has a BCC crystal structure and the interface that joins with the Nb phase is coherent (Ardeljan et al., 2018; Pathak et al., 2017). TEM analyses of the 7/7 nm composite reveal that the layer thicknesses in some regions in the same sample can range from 7 to 10 nm in Mg and 7 to 20 nm in Nb (Jain et al., 2021). The occasional larger Mg layer thicknesses close to 10 nm had an HCP crystal structure but a thin 1–2 nm BCC layer at the Mg/Nb interface(Jain et al., 2021). Since the strength of the composite is controlled by the lowest feature size (Misra et al., 2005; Pathak et al., 2015), these samples will be analyzed and modeled using their minimum layer thickness of 7/7 nm where Mg is in its pseudomorphic BCC crystal structure. Last, TEM analysis confirmed that largest layered nanolaminate has on average a Mg layer thickness of ~35 nm and a Nb layer thickness ~65 nm. An incoherent HCP/BCC interface joins the Mg and Nb phases.

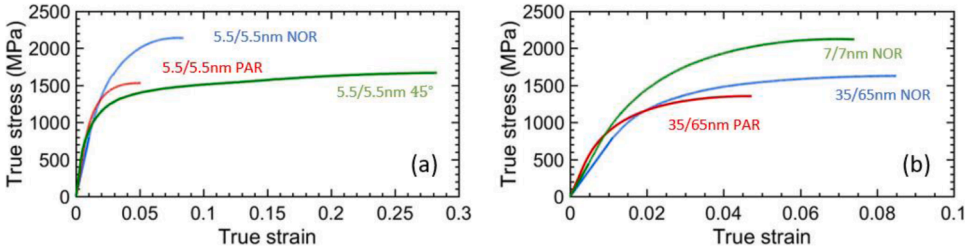

Fig. 2. Comparison of the true stress-strain responses between (a) Mg/Nb 5.5/5.5 and (b) Mg/Nb 35/65 nm and Mg/Nb 7/7 nm multilayered nanocomposites with interfaces oriented normal (isostress), parallel (isostrain) and 45° (shear) to the loading direction.

Table 1
Yield stress and Instability stress for three composites in different loading directions.

Layer-thickness	Compression direction	Yield stress (GPa)	Instability stress (GPa)
35/65 nm	Normal compression	1.05±0.9	1.80
	Parallel compression	0.83 ± 0.4	1.46
7/7 nm	Normal compression:	1.38 ± 0.11	2.30
5.5/5.5	Normal compression:	1.17 ± 0.01	2.48
	Parallel compression:	1.01 ± 0.04	1.62
	45° compression:	0.39 ± 0.2	0.70

To determine the plastic anisotropy of the composite stress-strain response, micropillar compression experiments were conducted on these nanolaminates. Details of the micropillar fabrication and in-situ SEM testing procedures are described in (Pathak et al., 2017). In brief, the micropillars were fabricated in the dual beam FEI Helios™ and Scios™ FIB Scanning Electron Microscopy (SEM), using a beam of Ga+ ions to remove the material and shape it in pillar form. Micropillars with layers oriented at three distinct angles with respect to the pillar axis (which is also the compression axis), 0° (normal), 45°, and 90° (parallel), were fabricated. Most of the micropillar stress-strain responses have been reported earlier (Ardeljan et al., 2018; Pathak et al., 2017), and here we additionally analyze the plastic flow response of the 7/7 nm the 0°orientation nanolaminate and the 5.5/5.5 nm 45°orientation nanolaminate.

3. Experimental results

Fig. 2 shows the true stress-strain curves of the 35/65 nm, 7/7 nm and 5.5/5.5 nm nanocomposites obtained from the micropillar compression tests. One representative stress-strain curve for each composite and loading orientation (normal, parallel and oblique 45°) is shown. The yield stress and instability stress of each stress-strain curve are listed in Table 1.

The plastic flow response of all but two of the responses have been discussed in prior works, but with the newly added curves a few aspects of the deformation response are worth noting. First, the flow stresses for the BCC Mg/Nb composites in all loading directions are higher than the HCP Mg/Nb composites. Both the 5.5/5.5 and 7/7 nm composites exhibit exceptionally high strength, especially in normal compression. In normal loading, the two BCC/BCC composite have similar hardening rate, while the 35/65 nm HCP/BCC Mg/Nb composite has a relatively lower hardening rate. Interestingly when the composites are loaded in the parallel orientation, the hardening rates between the 5.5/5.5 nm BCC/BCC and 35/65 nm HCP/BCC composites are similar, which is also similar to hardening rate of the 5.5/5.5 nm BCC/BCC composite in the 45° orientation. Second, the peak (or instability) strength generally increases with reduced layer thickness, from 1.80 to 2.30 GPa and 2.48 GPa in the normal direction, as the layer thickness h in Mg decreases from 35 nm, 7 nm, to 5.5 nm, respectively. This scaling in strength with reductions in h is frequently seen in nanolaminates (Mara and Beyerlein, 2014; Misra et al., 2005; Snel et al., 2017; Subedi et al., 2018). Notably, here, the scaling prevails across all composites, despite the changes in interface type and crystal structure that accompany the reduction in h. Third, the behavior of the BCC/BCC Mg/Nb and HCP/BCC Mg/Nb composites is plastically anisotropic, apparent most noticeably by the difference between the normal and parallel compression responses. The strength of the composite under layer-normal compression is consistently higher than under layer-parallel compression for the same layer thicknesses. For example, in the BCC/BCC Mg/Nb 5.5/5.5 nm composite the yield stress, the flow stress and the instability stress all have their highest values for the layer normal compression direction (see Table 1 and Fig. 2). The HCP/BCC Mg/Nb 5.5/5.5 nm composite also shows a similar trend between the normal and parallel orientations (see Table 1 and Fig. 2). Another important finding is that the difference of stress between the normal compression and parallel compression increases as the layer thickness decrease. For instance, for the 35/65 nm composite the percentage difference in the instability stresses between the normal and parallel orientations is ~24%, whereas for the 5.5/5.5 nm composite the difference is much larger, ~53%.

Table 2
Elastic moduli for the three phases in the Mg/Nb nanolaminates.

	C_{11}(GPa)	C_{12} (GPa)	C_{13}(GPa)	C_{33}(GPa)	C_{44}(GPa)
HCP Mg	59.5	26.1	21.8	65.6	16.3
BCC Mg	65	35	–	–	22.5
BCC Nb	246	134	–	–	28.7

4. Methodology

4.1. Basic CPFE framework

The CPFE framework is employed here as a method to calculate the stress-strain response of the Mg/Nb nanolaminates (Knezevic and Beyerlein, 2018; Knezevic et al., 2014). In brief, a 3D two-phase polycrystalline laminate structure is constructed of finite elements. At each finite element integration point, the material constitutive response is modeled utilizing CP theory by Kalidindi et al. (1992). In application of the CP theory, plastic strain is realized by simultaneous action of crystallographic slip on multiple slip systems. Below, we briefly review the formulation, then follow with the construction of the 3D laminate model and its properties, and the simulation boundary conditions.

The following description adopts standard continuum mechanics notation, where tensors are denoted using roman boldface symbols, while scalars are italicized and not boldfaced. A dot is placed over a particular quantity to represent a time derivative.

A global stress equilibrium solution for each step is found using the numerically iterative procedure of the FE method. This end is achieved by solving the nonlinear FE governing equation in its linearized form given by

$$\left(\int_V \mathbf{B}^T \mathbf{J}\mathbf{B} dV\right)\Delta\mathbf{U} = \mathbf{R} - \int_V \mathbf{B}^T\boldsymbol{\sigma} dV \tag{1}$$

In this relation, $\mathbf{B}$ is the FE strain-displacement matrix, $\mathbf{J}$ is the material Jacobian matrix, $\Delta\mathbf{U}$ is the displacement increment solution, $\mathbf{R}$ is the applied force vector and $\boldsymbol{\sigma}$ is the Cauchy stress tensor (Ardeljan et al., 2014, 2015; Bathe, 1996; Knezevic and Beyerlein, 2018; Zecevic et al., 2015a, 2015b).

An essential part of CPFE is the CP constitutive law, which links the material stress with material distortion at each FE in the model microstructure. The finite deformation CP-based formulation used here is based on the one developed in Kalidindi et al. (1992). We begin with the decomposition of the total deformation gradient tensor $\mathbf{F}$ into elastic and plastic components according to

$$\mathbf{F} = \mathbf{F}^*\mathbf{F}^{\mathbf{P}} \tag{2}$$

where $\mathbf{F}^*$ encompasses the deformation gradients due to both elastic stretching, as well as lattice rotation, while $\mathbf{F}^{\mathrm{P}}$denotes the deformation gradient due to plastic deformation. The constitutive relationship between $\mathbf{F}^*$and $\boldsymbol{\sigma}$ is given by:

$$\mathbf{T}^* = \mathbf{C}\mathbf{E}^* = \mathbf{F}^{*^{-1}}\ \{(\det\mathbf{F}^*)\boldsymbol{\sigma}\}\mathbf{F}^{*^{-1}}, \mathbf{E}^* = \frac{1}{2}\left\{\mathbf{F}^{*^T}\mathbf{F}^* - \mathbf{I}\right\} \tag{3}$$

where $\mathbf{C}$ is the fourth order elasticity tensor. Tensors $\mathbf{T}^*$ and $\mathbf{E}^*$ are the work conjugate stress and strain measures, respectively. The plastic deformation gradient $\mathbf{F}^{\mathrm{P}}$ evolves according to plastic slip at each material point via:

$$\dot{\mathbf{F}}^{\mathrm{P}} = \mathbf{L}^{\mathrm{P}}\mathbf{F}^{\mathrm{P}},\ \mathbf{L}^{\mathrm{P}} = \sum_s \dot{\gamma}^s\left(\mathbf{b}_0^s \otimes \mathbf{n}_0^s\right),\quad \mathbf{F}^{\mathrm{P}}(\tau) = \{\mathbf{I} + \Delta t\mathbf{L}^{\mathrm{P}}(\tau)\}\mathbf{F}^{\mathrm{P}}(t) \tag{4}$$

where $\dot{\gamma}^s$ is the slip rate on slip system s, $\mathbf{b}_0^s$ and $\mathbf{n}_0^s$ are slip direction and slip plane normal of the slip system, and $\mathbf{I}$ is the second-rank identity tensor. The tensor $\mathbf{L}^{\mathrm{P}}$ is the plastic velocity gradient.

The $\dot{\gamma}^s$ for each slip system s is related to the resolved shear stress on the same system given by $\tau^s = \mathbf{T}^* \cdot \mathbf{m}_0^s$, where $\mathbf{m}_0^s = \mathbf{b}_0^s \otimes \mathbf{n}_0^s$ is its Schmid tensor according to the following power-law relationship (Asaro and Needleman, 1985; Hutchinson, 1976; Kalidindi, 1998):

$$\dot{\gamma}^s = \dot{\gamma}_0\left(\frac{|\tau^s|}{\tau_c^s}\right)^{\frac{1}{m}} sign(\tau^s) \tag{5}$$

In Eq. (5), τ_c^s is a characteristic resistance to slip, $\dot{\gamma}_0$ is a reference slip rate (arbitrarily taken here as 0.001 s^{-1}), and m is the strain sensitivity parameter (taken as 0.02).

4.2. Elastic and plastic properties of the Mg and Nb phases

The elasticity HCP Mg phase is transversely isotropic and the five elastic constants in its elasticity tensor $\mathbf{C}$ are given in Table 2. The elasticity of the BCC phases is cubic anisotropic and the three elastic constants of the elasticity tensor $\mathbf{C}$ for BCC Mg, and BCC Nb used in the simulation are also given in Table 2. For the natural HCP Mg and BCC Nb phases, the values are reported from experimental studies

Table 3
Slip systems made available to the crystal plasticity model for accommodating plasticity in the nanolaminates.

35/65 nm	Basal ($\alpha = 1$)	$\{0001\}\langle 1\bar{2}10\rangle$	BCC Nb($\alpha = 1$)	$\{011\}\langle 11\bar{1}\rangle$
	Prismatic ($\alpha = 2$)	$\{10\bar{1}0\}\langle \bar{1}2\bar{1}0\rangle$	BCC Nb($\alpha = 2$)	$\{112\}\langle \bar{1}\bar{1}1\rangle$
	Pyramidal ($\alpha = 3$)	$\{11\bar{2}2\}\langle 11\bar{2}3\rangle$		
7/7 nm 5.5/5.5 nm	BCC Mg($\alpha = 1$)	$\{011\}\langle 11\bar{1}\rangle$	BCC Nb($\alpha = 1$)	$\{011\}\langle 11\bar{1}\rangle$
	BCC Mg($\alpha = 2$)	$\{112\}\langle \bar{1}\bar{1}1\rangle$	BCC Nb($\alpha = 2$)	$\{112\}\langle \bar{1}\bar{1}1\rangle$

(Bolef, 1961; Slutsky and Garland, 1957), while those for BCC Mg were characterized in (Su et al., 2020). The slip families made available in the simulation are listed in Table 3. Deformation twinning was not considered since twins were not detected via post-mortem TEM analysis and the conventional signatures of twinning in HCP metals, such as an increase in hardening rate with strain, did not appear in the stress–strain curves. Additionally, the back stress due to the geometric and elastic/plastic constraints of the adjacent Nb layers are known to impede nucleation and/or thickening of twins in the Mg layer, and twinning in Mg in a Mg/X nanolaminate has not yet been observed in literature (Chen et al., 2019).

4.3. Dual-mode CLS law

The flow rule in the constitutive law used in CPFE requires a value for τ_c^s in order to activate slip on slip system s. As shown in Table 3, the BCC and HCP phases deform by multiple slip modes, two for BCC and three for HCP. Here for τ_c^s we introduce a hardening law for the evolution of τ_c^s with strain. There are two primary contributions to the τ_c^s: a non-evolving resistance, which is independent of the interactions with other dislocations and the interfaces, and another component, $\tau_{disl}^s(h^s)$, which depends on layer thickness. Combined the τ_c^s is given by:

$$\tau_c^s = \tau_0^\alpha + \tau_{disl}^s(h^s) \; s \in \alpha \tag{6}$$

In the formulation, we use superscript α to denote quantities that apply to all slip systems belonging to the same slip mode (i.e., $s \in \alpha$) and superscript s to those that only apply to the specific slip system s. The resistance τ_0^α for a nanocrystal could be very different than the slip strengths for traditional polycrystals. It can be closer to the critical stress to activate small nm sources and can be generally higher than the values encountered in coarse-grained defective crystals.

The second term, $\tau_{disl}^s(h^s)$ represents the resistance to glide imposed by the closely spaced interfaces and is a direct function of layer thickness h. The common model for glide resistance assumes that dislocation density accumulates uniformly within the layers. In the present composites, the concept of a homogeneous distribution of accumulated dislocation density does not apply to layers of nanoscale dimensions. Physically, the nm interface spacing is usually less than one order of magnitude greater than the dislocation core itself, indicating that slip is heterogeneous. As confirmation, in previous experiments (Ardeljan et al., 2018; Pathak et al., 2017), postmortem TEM analysis did not observe dislocation storage in the composite. Therefore, the glide resistance for dislocations moving within layers of nanoscale dimensions needs to account for the resistances from other sources, such as their interactions with surfaces, interfaces, and grain boundaries that confine them.

To this end, the confined layer slip (CLS) law has been proposed to represent the slip resistance when interfaces confine the movement of the dislocations, forcing them to bow out between the two adjacent interfaces, in the MNC (Misra et al., 2005, 1999). Later, the CLS model was extended to account for energetic expense associated with depositing dislocations within the interfaces thread through (Misra et al., 2005, 1999; Nix, 1989). In the conventional application of the CLS law, the CLS size effect is usually directly translated to explain the size effect in the macroscopic strength or hardness of the nanolayered composite (Misra et al., 2005, 1999). Recently in a few works, the basic CLS model is applied to redefine the critical resolved shear stress (CRSS) used for every slip system and incorporated into the constitutive law of a CPFE model (Ardeljan et al., 2018; Liu et al., 2019). In Ardeljan et al. (2018), two orientations were modeled, but yet still it was found that the standard CLS form was not applicable to general loading directions and the origins of strengthening could not be identified.

At these fine scales, in addition to the interactions of moving dislocations with nearby interfaces, the orientation of the dislocation glide planes with respect to the interface also needs to be considered. In all MNCs studied here, the interface planes are also dislocation glide planes. Accordingly, for certain orientations of the crystal, some glide planes could, therefore, lie parallel to the interface and, accordingly would be unaffected by the interface and layer thickness. Consequently, CLS has two distinct modes. One mode is the traditional one, wherein the dislocations gliding on planes that are non-parallel to the interface. The second mode pertains to the dislocations gliding on planes parallel to the interface, which do not interact with the interface. These parallel dislocations, are, however, constrained, by the in-plane grain boundaries. Here, the hardening model in Eq. (6) is extended to account for these two modes and we refer to this modified CLS law as the dual-mode CLS law. Its account for orientation-dependent resistance enables prediction of the anisotropic response of MNCs when tested in all possible orientations of the glide planes with respect to the interface. Below we describe each mode in the dual-mode CLS law in turn.

In the first mode, the dislocation slip plane is not parallel with the interface between two layers. To identify the inclined slip planes, the angle θ between the slip direction in the slip plane and layer interface normal is calculated. Angles smaller than 85° are associated with inclined planes and vice versa for parallel planes. In this case, the threading dislocation can experience a resistance to slip that

increases as the layer thickness h decreases. This mode provides a direct size effect to slip resistance. The generalized form of the CLS model used here is given by

$$\tau^s_{disl}(h^s,\alpha,s)=\tau^s_{CLS}\left(\frac{h^{s'}}{b^\alpha}\right)=\frac{{A_{int}}^\alpha\mu^\alpha b^\alpha}{h^{s'}}\ln\left(c\frac{h^{s'}}{b^\alpha}\right),\ s\in\alpha \tag{7}$$

where $h^{s'}$ is the distance along the slip plane of slip system from one interface to the next. This crystallographic thickness $h^{s'}$ depends on the orientation of the crystal with respect to the interface normal and the layer thickness h. The parameter c is the core-cut off parameter that ranges from unity to $\sqrt{2}$ and is set to $\sqrt{2}$ in the calculations that follow. The b^α is the magnitude of Burgers vector and μ^α is the effective isotropic shear modulus. The coefficient ${A_{int}}^\alpha$ is related to the self-energy of the dislocation from slip mode α deposited in the interface. It will depend on the type of interface: sharp coherent or sharp incoherent or the mixed interface formed as a natural consequence of the mixed HCP-BCC Mg phase in the 7/7 nm composite. The $ln(h)/h$ dependence in $\tau^s_{disl}(h^s)$ results from the resistance due to line tension as the dislocation bows out between the layers.

In the second mode, the slip plane is parallel with the layer interface. In this case, the constraint against the movement of dislocation is provided by the in-plane grain size d, spanning from one grain boundary to the next. This value varies from grain to grain in the material but for simplicity, we assume that the size distribution can be well represented by an average or equivalent in-plane d. On this basis, for the second mode, the GB affected resistance is given by

$$\tau^s_{disl}(h^s,\alpha,s)=\tau^s_{CLS}\left(\frac{h^{s'}}{b^\alpha}\right)=\frac{{A_{GB}}^\alpha\mu^\alpha b^\alpha}{d}\ln\left(c\frac{d}{b^\alpha}\right),\ s\in\alpha \tag{8}$$

where the coefficient ${A_{GB}}^\alpha$ denotes the self-energy of a dislocation belonging to slip mode α deposited in the grain boundary. It depends on the material, whether HCP Mg, BCC Mg, or BCC Nb. Other terms retain the same definition as Eq. (6). Following measurement from TEM, the average d is taken to be 100 nm in the simulation.

In the model, τ_0^α, A_{int}^α, and A_{GB}^α are characterized such that all the strain-stress curves from the multiscale model agree with the measured strain-stress curve. Particular interest lies in identifying A_{int}^α for the coherent interface, thin coherent BCC interphase, and incoherent interface in order to assess the strengthening effects of interface type. To condense the parameter set down to contain only the essential physical quantities, we elect to make a few more assumptions. First, Nb is the same in all three types of composites and thus, have the same values for τ_0^α and for the grain boundary ${A_{GB}}^\alpha$. Second, the τ_0^α depends on mode and does not vary among the slip systems belonging to the same mode. Third, we consider the differences between τ_0^α for the {110} ⟨111⟩ and {112} ⟨111⟩ slip modes to be relatively small compared to differences between τ_0^α for Mg and Nb. Therefore, a single τ_0^α is shared for both BCC slip modes in the same phase. While important, the screw/edge dependence on τ_0^α or non-Schmid effects in these BCC slip modes is also not considered (Cho et al., 2018; Weinberger et al., 2012). Consequently, the value of τ_0^α obtained will likely be more representative of the screw dislocations, which are much harder to move than the non-screw components. Next, we consider that A_{int}^α and A_{GB}^α are the same for all types of dislocations belong to the phase. Last, for the 7/7 nm composite, we treat it as a BCC/BCC composite with a potentially different value of A_{int}^α, to represent the possibility that small fractions of the interface are incoherent.

5. 3D model microstructure

The 3D microstructure model for the CPFE calculation was constructed to be as close as possible to those of the MNCs. The individual polycrystalline layers containing representative grain shapes were first generated through Dream.3D then assembled in a large-scale voxel-based model using a Matlab script. Surface meshing filters implemented within DREAM.3D were then performed to generate the surface meshes of all the individual grains. Next, a Laplacian based smoothing filter is applied to smooth the serrate boundaries between the grains. We then proceed with performing solid meshing of the interior of each and every grain in MSC Patran. Finally, we generated an FE model of the granular microstructure that is composed of linear tetrahedral C3D4 elements. This process was applied without adjustment to create the microstructures for the parallel and normal tests. The meshing procedures have been described in Barrett et al. (2018) and Knezevic et al. (2014).

For the test samples with interfaces inclined 45° to the compression axis, a different step is employed after the individual layers are generated in Dream.3D. Instead of a single bilayer, multiple layers were assembled using the Matlab script. The assembly is then cut by selecting voxels from the interior (see Fig. A1 in the Appendix). The cutting profile was defined such that the layers are inclined 45° with respect to the global axes. Afterwards, we proceeded with the process of surface and solid meshing. The model for the 45° 5.5 nm/5.5 nm composite is shown in Fig. A2 in the Appendix. It contains 20 layers and roughly 1 million C3D4 (continuum three-dimensional four-nodal) elements. The dimensions of this model when scaled with respect to the individual layer thickness are 401, 466, 184 nm in the *x, y, z* directions.

The finer BCC Mg nanolaminates were modeled as having equal Mg and Nb layer thicknesses of 5.5 and 7 nm. As mentioned earlier, although the 7/7 nm composite has a range of layer thicknesses for both Mg and Nb, the minimum layer thickness of 7 nm is expected to control the strength of the composite. Hence this composite was modeled with a 7 nm layer thickness. The larger layered 35/65 nm composite was represented by unequal layer thicknesses of 35 nm for the Mg layer and 65 nm for the Nb layer. While TEM results have indicated that there is a possibility of a thin 1–2 nm pseudomorphic BCC layer at some regions of the Mg/Nb interface in the 35/65 nm composite, these regions represent a negligible volume fraction of the overall composite.

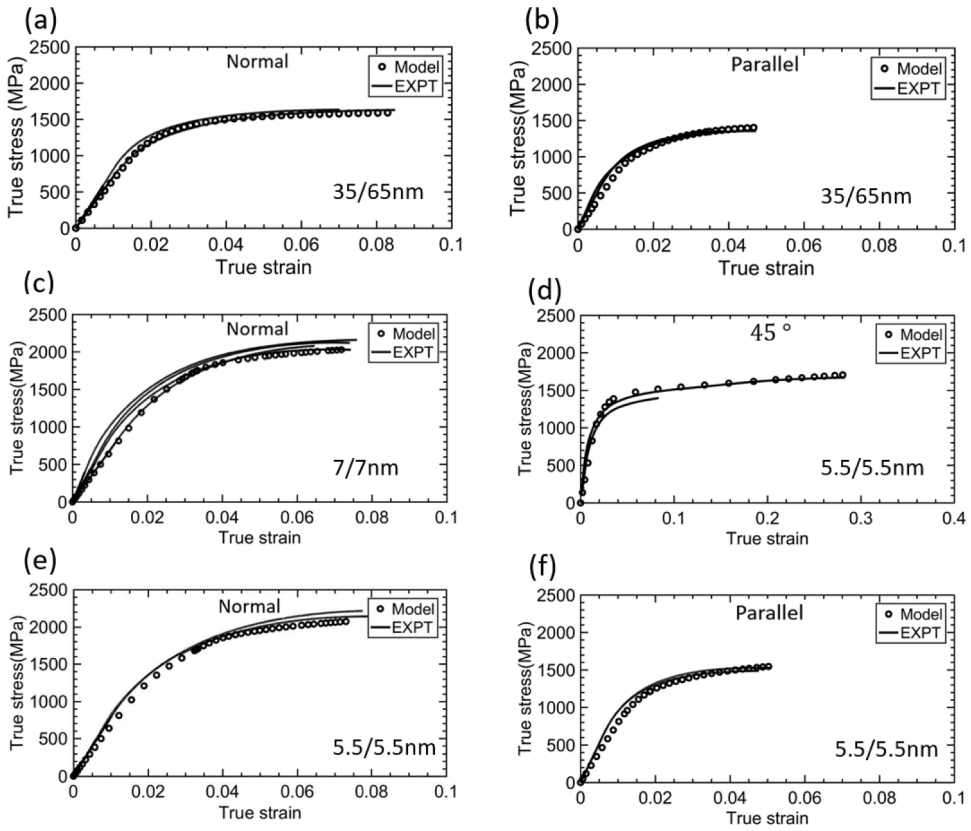

Fig. 3. Comparison of the mechanical stress-strain responses from modeling and experiments (see Fig. 2 for the experimental stress-strain graphs) of the multilayered composites (a). 35/65 nm normal compression; (b). 35/65 nm parallel compression; (c). 7/7 nm normal compression; (d) 5.5/5.5 nm oblique 45° compression; (e) 5.5/5.5 nm normal compression; (f) 5.5/5.5 nm parallel compression.

All layers are polycrystalline in-plane and single crystalline through thickness with one grain spanning the layer thickness. In the 35/65 nm model, the Mg and Nb grains have a low aspect ratio ranging from 2 to 3, being 100 nm wide in-plane and with a thickness equal to its own layer thickness. In the 5.5/5.5 nm model and 7/7 nm composites, however, while the layer h is reduced to 5.5 and 7 nm, the in-plane cross-sectional shape and in-plane grain d of 100 nm are retained. Fig. A3 in the Appendix shows representative volumes of the meshed bilayer of Mg and Nb for the 35/65, 7/7, and 5.5/5.5 nm samples. In these models, the grain microstructure is periodic. The FE meshes consist of roughly 600,000, 1000,000 and 435,000 C3D4 elements, in the 35/65, 7/7 and 5/5 nm cases, respectively. When scaled with respect to the individual layer thickness, the length and width of the 35/65 and 7/7 nm models correspond to 1000 nm and of the 5/5 nm model 1650 nm.

The grain orientations in the model microstructures were randomly selected from the corresponding initial XRD measured texture in Fig. 1. For the 7/7 and 5.5/5.5 nm composites, following experimental measurements, the BCC Mg phase and BCC Nb have the same initial texture as the BCC Nb phase in the 35/65 nm composite. Since the Mg phase in the 7/7 nm composite may have non-negligible volume fractions of the HCP phase, we later construct an alternative model of the 7/7 nm composite in which the Mg phase is HCP with a thick BCC Mg interphase and discuss the ensuing implications.

We simulate compression deformation in all microstructural models (Jahedi et al., 2015). In the loading direction, the displacement is prescribed, while the lateral faces were kept free to expand. The grain microstructure is fully periodic for normal and parallel models, while only the layered structure (not grain structure) is periodic for the 45° model. The loading applied normal and parallel to the Mg/Nb interfaces is compressive in the z- and x-directions, respectively. Boundary conditions are such that the deformation of each pair of boundary faces (top/bottom, front/back, and left/right) is equal and the stress tensors on each pair are opposite in sign. In the 45° model, compression is only applied in the x-direction.

The single crystal constitutive law at each integration point is written as a user-defined material (UMAT) subroutine and implemented into the finite element software Abaqus (Kalidindi et al., 1992, 2006). In a given deformation simulation, the applied deformation is divided into time/strain increments. As output, the model calculates at every increment the crystallographic orientation, slip activity, and intergranular and intergranular stress, strain rate, and strain fields.

Table 4
Material parameters for the HCP Mg/BCC Nb nanocomposites.

	Mg			Nb	
Slip mode	Basal	Prismatic	Pyramidal	{011}	{112}
τ_0^α	100	160	240	485	485
A_{int}^α	1.0	1.0	1.0	0.35	0.35
A_{GB}^α	1.0	1.0	1.0	0.157	0.157

Table 5
Material parameters for the BCC/BCC Mg/Nb nanocomposites.

	Mg		Nb	
Slip mode	{011}	{112}	{011}	{112}
τ_0^α	185	185	485	485
A_{int}^α	0.097–0.127	0.097–0.127	0.187	0.187
A_{GB}^α	0.087	0.087	0.157	0.157

6. Results

6.1. Stress–strain response

The dual-mode CLS model within CPFE microstructure is applied to simulate the deformation of 35/65, 7/7 and 5.5/5.5 nm Mg/Nb composite from the beginning of loading to the peak stress. Fig. 3 compares the experiment results with the calculated ones using the material parameters in Tables 4 and 5. As shown, in each test, calculated stress-strain responses achieve good agreement in yield stress and hardening rate for all curves.

6.2. Material and interface properties

The key set of local material and interface parameters are characterized such that they reproduce the stress-strain response for the entire straining period for all samples. The parameters should transcend texture, layer thickness, and loading orientation, such that a single set of parameters can be used as long as the material composition and interface do not change. When analyzing these model parameters, a key question of interest is how the plastic properties of Mg change from the stable HCP state to the metastable BCC pseudo-morphic state, independent of the interface. This can be address by analyzing the slip strength τ_0^α. For the HCP Mg phase, the τ_0^α are found to be much lower for <a> slip than <c+a> slip, a trend consistent with many prior studies on bulk HCP Mg alloy studies (Ardeljan et al., 2018; Kumar et al., 2017a, 2017b; Lentz et al., 2016; Risse et al., 2017; Savage et al., 2020). Second, a single value of τ_0^α is found for both <111> slip modes in BCC Mg, for which there are 24 slip systems. This τ_0^α resistance for BCC Mg <111> slip is higher than that of <a> slip in Mg. Therefore, the BCC Mg phase, not only becomes stronger, but it naturally lowers its slip plane anisotropy, since the CRSS values among slip modes of a pure BCC metal are closer in value than those of a pure HCP metal. Another notable result is that a single effective value for τ_0^α in the Nb phase could be obtained for all composites. This value in Nb is higher than that of BCC Mg. Its value is relatively high, and likely reflects the resistance of the screw-character portions of the dislocation loops than the non-screw parts. For reference, DFT calculations at 0 K have estimated that the Peierls stress for screw dislocations is 740 MPa (Weinberger et al., 2013). Therefore, for all types of Mg/Nb composites studied here, we find that Nb remains the harder phase.

While the τ_0^α strength is unaffected by the interface and its properties, the two interface coefficients ${A_{int}}^\alpha$ and ${A_{GB}}^\alpha$ pertain directly to the local change in the core of the dislocation when deposited in the interface and grain boundary, respectively. They directly reflect the effect of interface type resisting propagation of a dislocation in the layers. First, we notice that the contribution of grain boundaries is less than or equal to the interface. For HCP Mg, the resistance to all dislocations by grain boundaries and the incoherent interface alike is the highest among the other cases of dislocations in simple cubics or with coherent interfaces. Next, we find that ${A_{int}}^\alpha$ is much higher, by an order of magnitude, for the incoherent interface in the HCP/BCC 35/65 nm composite compared with the coherent (or mostly coherent) bimetal interface in the BCC/BCC composites. This implies that the HCP/BCC incoherent interface much more strongly resists the interaction with the moving lattice dislocation than the coherent BCC/BCC interface.

6.3. Slip activity in the Mg and Nb phases in deformation

The model can be used to predict the slip activities in each crystal at each strain level. We first analyze the relative contributions of parallel vs. non-parallel interface glide. Their relative activities are calculated as the average slip rate of each mode to the total slip rate in each grain. In all cases, non-parallel dislocation activity dominates. Due to the orientation of the crystals relative to loading, the resolved shear stress is non-zero on the glide planes inclined to the interface planes. For the BCC/BCC composites, interface-parallel glide accommodates less than 2% of the deformation, while for the HCP/BCC composites, it accommodates about 10%. Even in the 45°

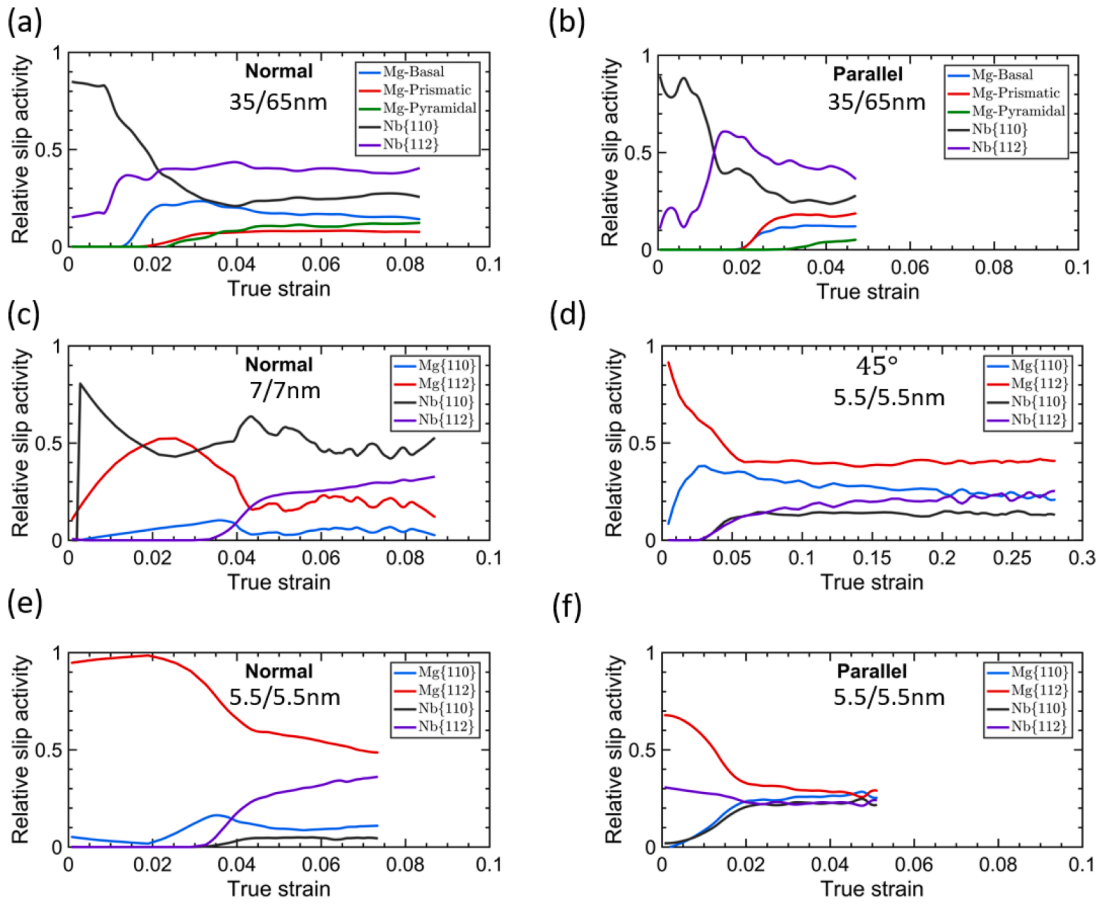

Fig. 4. Calculated slip activities in the HCP Mg/Nb and BCC Mg/Nb nanocomposites (a). 35/65 nm normal compression; (b). 35/65 nm parallel compression; (c). 7/7 nm normal compression; (d) 5.5/5.5 nm oblique 45° compression; (e) 5.5/5.5 nm normal compression;(f) 5.5/5.5 nm parallel compression.

5.5/5.5 nm composite test, the amount of parallel glide is the same as in the normal and parallel tests. The greater parallel glide contribution in the HCP composite results from the substantially weaker lattice resistance for basal <a> slip that lies parallel to the basal interface plane in the HCP/BCC composite than the other HCP slip modes that lie non-parallel to the interface. In contrast, in the BCC/BCC composite, the lattice resistances are the same for all modes. Last, the propensity for non-parallel glide has implications on the strength of the layer-size effect. Non-parallel glide is directly affected by the layer thickness, whereas parallel glide is independent of it. It can, therefore, be expected that the pseudo-morphic Mg/Nb MNCs are more sensitive to changes in layer thickness than the regular HCP/BCC MNCs.

Fig. 4(a) and (b) show the relative activities of the three slip modes in HCP Mg and two slip modes in BCC Nb in the HCP/BCC MgNb composite under normal and parallel compression. The relative slip activity is defined as the average contributions of the slip rate for each slip mode to the deformation. The results show that initially slip begins in the Nb phase and develops later in the straining in the Mg phase. The two reasons for this are that the volume fraction of Nb phase is larger than that of the Mg phase, and incoherent HCP/BCC interface acts as a much stronger obstacle against all dislocation types in the Mg phase ($A_{int}{}^{\alpha} = 1$) than those in the Nb phase ($A_{int}{}^{\alpha} = 0.35$). In the Mg phase, we observe that, initially, basal slip is the dominant deformation mode, while pyramidal slip contributes the least, in both loading configurations. This can be expected as basal slip has the lowest τ_0^{α} of the three modes. Another observation pertaining to the Mg phase is that basal slip contributes more in normal compression, while prismatic slip contributes more in parallel compression. In the Nb phase, the slip activities in Fig. 6(a) and (b) in the two loading orientations are similar. The {110} slip mode dominates the deformation in the early stages of straining, while the {112} model prevails and becomes dominate in the later stages.

In BCC/BCC MgNb composites, the slip activities are completely different than in the HCP/BCC composites. The first notable difference is that the Mg phase accommodates most of the deformation compared to the Nb phase. In these two composites, the Mg and Nb phases have equal volume fraction and the interfaces impose less resistance on the {112}<111> and {110}<111> dislocations from Mg ($A_{int}{}^{\alpha} = 0.1$) than on the same dislocations in Nb ($A_{int}{}^{\alpha} = 0.19$). However, with straining, in all three loading orientations, eventually both slip modes contribute to accommodating deformation. In the parallel test, the Mg and Nb phases are co-deforming, as signified by the similar contributions of all four slip modes. In contrast, in the normal and in the 45° tests, the relative slip activity of

dislocations in Nb is initially (in early stages, less than 0.02 strain) negligible. In the parallel case, co-deformation is promoted by the approximate "isostrain" conditions (equal strain in both phases). The normal case, however, represents nearly "isostress" conditions and the 45° case, an approximate shear mode, and thus, most of the deformation is taken up by the weaker Mg phase. Both slip modes {110} and {112} in the Mg phase dominate throughout deformation. Because the two modes {110} and {112} have the same initial resistance τ_0, and interactions with the grain boundary and interfaces (e.g., reflected by coefficients ${A_{int}}^{\alpha}$, and ${A_{GB}}^{\alpha}$), the preferences in activation between the {110} and {112} modes are a result of their differences in orientation. In addition, the two phases have the same initial texture, and consequently, the favored slip mode should be the same initially in both the Mg and Nb phases. As seen in Fig. 4(c)–(e), the {112} slip mode is the major deformation mode in the Mg and Nb phases during normal compression.

7. Discussion

7.1. Interface between Mg and Nb phase in 7/7 nm composite

The mixed phase 7/7 nm nanocomposite is modeled here as a predominantly BCC/BCC composite with a largely coherent interface. X-ray diffraction and deformation modeling results indicate that the layer is mostly pseudomorphic BCC Mg phase and this phase contributes to the strength of the composite via highly resistance to <111> slip. Nevertheless, the occasional HCP Mg phase mixed with the BCC Mg phase could render some portions of the interface incoherent. The model suggests that the mixed effect manifests as a slight raise in the coefficient ${A_{int}}^{\alpha} = 0.127$, signifying a slightly higher resistance to dislocation propagation.

Alternatively, we could have assumed that the 7/7 nm composite is an HCP/BCC Mg/Nb composite with special BCC Mg interphase, a few nanometers thick, lying in-between the HCP Mg layer and BCC Nb layer. To represent this nanostructure, we model the 7/7 nm composite as an HCP Mg phase bound to a BCC Nb phase and adopt for the HCP Mg phase, the same material and grain boundary parameters of the HCP/BCC composite as listed in Table 4. We only recharacterize a coefficient ${A_{int}}^{\alpha}$ associated with the BCC Mg interphase. We find that ${A_{int}}^{\alpha} = 2$ provides a stress-strain response in agreement with the measured 7/7 nm response. This value is twice as high as a sharp incoherent interface. While we cannot confirm the HCP Mg/interphase Mg/BCC Nb nanostructure prevails over the entire nanocomposite, this result would indicate that the BCC Mg layer poses a much greater resistance against the motion of dislocations in Mg than a sharp HCP/BCC interface.

7.2. Plastic anisotropy of BCC/BCC composite

Considering the mechanical responses in Fig. 3, an interesting finding is substantial differences between the stress-strain responses of the three loading orientations of the BCC/BCC 5.5/5.5 nm composite. The normal compression response has the highest hardening rate and strength, and the 45° compression has the lowest ones. Such significant plastic anisotropy is usually explained by differences of crystallographic orientations of the grains with respect to the loading direction or texture or plastic anisotropy in the HCP phase. In this composite, both phases are BCC and the two slip modes in the same phase have the same strength. Thus, the plastic anisotropy in the macroscopic response arises not from differences in material slip strengths but from the different orientations of the layers with respect to the loading axis in the three tests. Comparing Fig. 4(c)–(e), we observed that in normal compression, the contribution of Nb {112} slip is high compared to that in the other two directions. The dominance of this mode largely explains the high flow stress and high hardening rate seen in normal compression, since Nb is the harder phase in this 5.5/5.5 nm composite. In 45 °compression, however, Mg {110} slip is actively contributing to the deformation, particularly in the early stages, while in the normal and parallel tests, this mode does not. This difference could explain why 45° compression has the lowest hardening rate since between Nb and Mg, the τ_0^{α} of Mg {110} is low and the interface and grain boundaries in Mg pose a lower resistance to the dislocations in Mg. The different layer orientations also change how the layer thickness h evolves with strain. During the deformation, normal compression experiences the most severe reduction in h, which results in a higher CRSS. This hardening effect also contributes to the highest strength achieved in normal compression. Compression in the 45° test also causes a reduction in h with straining but to a smaller degree than in the normal test. In contrast, the layer thickness increases in the parallel compression test with straining, following volume conservation. This effect further decreases the strength of parallel relative to the other two orientations.

7.3. Origins of the high strength of the BCC Mg/Nb MNCs compared to HCP Mg/Nb MNCs

A question that arose earlier concerns the origin of the observed high strength of the BCC Mg/Nb composites compared with the HCP Mg/Nb composites. Between these two types of composites the interface, layer thicknesses, and phase structures are different. With the 3D CPFE microstructural model incorporating the dual-mode CLS model, we are able to separate effects of interface type, layer thickness, and crystal structure (BCC vs. HCP), furthermore identify key strengthening mechanism.

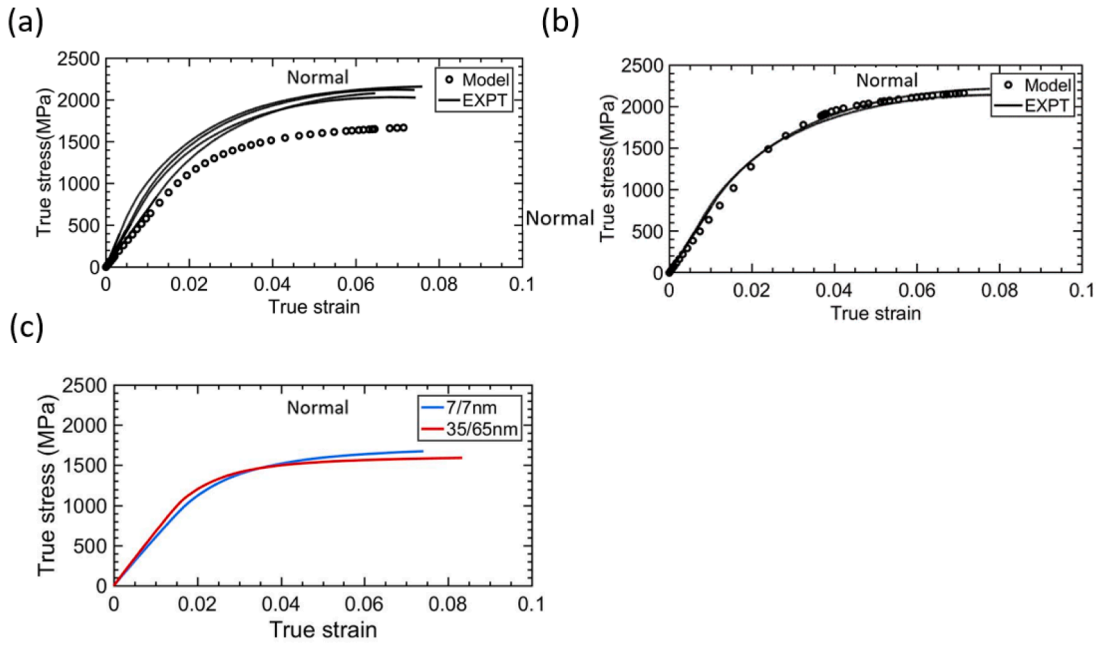

Fig. 5. Simulation of compression in normal direction (a) 7/7 nm HCP/BCC composite with parameters for 35/65 nm composite; (b) 5.5/5.5 nm composite with parameter for 7/7 nm; (c) Comparison of the HCP/BCC composites with 7/7 nm layer thickness and 35/65 nm layer thickness.

First, we examine the effect of crystal structure, which possess different slip modes and their associated initial slip resistances. This comparison is not straightforward since the HCP Mg has three slip families that are distinct from the two families in BCC Mg. We see that the initial resistance of basal <a> slip and prismatic <a> slip is lower than the initial resistance of two slip modes in the BCC Mg phase. As long as the <a> slip modes are just as active as the <111> slip modes, then the pseudomorphic phase transformation itself leads to strengthening. The BCC phase is overall stronger than its stable HCP phase. At the same time, it important to note the prediction of slip activity in Fig. 4. In the compression tests, none of the three deformation modes in HCP Mg contribute much to the deformation and most of the deformation is accommodated by the Nb. The opposite is true in the BCC/BCC composite, wherein the pseudomorphic phase contributes more than the Nb phase. Thus, it suggests the increase in the intrinsic glide resistance from <a> slip in the HCP Mg phase to the [112} and {110}<111> slip in BCC Mg is one main reason for strengthening.

As a test, we forecast the strength of the 7/7 nm composite as an HCP/BCC composite, under the supposition that the pseudomorphic transformation did not occur and the Mg phase remained in its HCP structure and hence the interface remained incoherent. Fig. 5(c) compares the calculated stress-strain responses for the 35/65 nm and 7/7 nm for the two HCP/BCC composites. As shown, the reduction in layer thickness did not lead to a significant increase in strength, in contrast to the significant increase seen when the Mg phase undergoes the pseudomorphic phase transformation. The reason, as explained above, is that the Nb accommodates most of the strain and a good fraction of the slip activity entails basal <a> slip parallel to the interface plane and hence is not size dependent. For further consideration, Fig. 5(a) compares the hypothetical 7/7 nm HCP/BCC composite with the calculated 7/7 nm for the actual BCC/BCC composite, identifying a substantial drop in the strength compared to experiment should the Mg phase in the composite remain HCP.

Second, we investigate the effect of biphase interface type, setting aside the effects of grain boundaries, since those are equivalent in the two composites. The HCP/BCC composite has an incoherent interface, while BCC/BCC composite has a coherent interface. The coefficient $A_{int}{}^{\alpha}$, representing the dislocation/interface interaction identifies that the incoherent HCP/BCC interface provides the higher resistance. For Nb, for the same dislocations, we find that $A_{int}{}^{\alpha}$ is higher for their interaction with the incoherent interface (0.35) than the coherent interface (0.187). For Mg, the differences in $A_{int}{}^{\alpha}$ are greater from 1.0 for the incoherent interface to ~0.1 for the coherent interface. However, we still need to bear in mind that the types of dislocations interacting with these interfaces are also different. Thus, given the order of magnitude difference, it is reasonable to conclude that the incoherent interfaces are the stronger interface against dislocation threading. Further, by comparing $A_{GB}{}^{\alpha}$, we can see that the grain boundaries in HCP Mg impose a higher resistance to <a> and <c+a> dislocations than those in BCC Mg to the {110} and {112} dislocations. The change in the interface type from incoherent to coherent in the pseudomorphic phase transformation did not contribute to strengthening.

Third, the BCC/BCC composites have a much finer layer thickness h, which we can anticipate provides substantial strengthening by increasing the resistance to dislocation CLS, with all else being the same. This CLS effect has been directly incorporated into the dual-mode CLS law in Eq. (6). The 7/7 nm composites had a higher $A_{int}{}^{\alpha}$, due to the mix phased interface. If this type of interface was retained as the layer thickness reduced to 5.5/5.5 nm, then the composite would be even stronger. Fig. 5(b) shows a prediction from the simulation of a 5.5/5.5 nm composite with the $A_{int}{}^{\alpha}$ interface coefficient. The calculations indicate that the composite would be slightly stronger if the mixed phase was preserved. Therefore, the reduction in h from 7 nm to 5.5 nm helped to strengthen the 5.5/5.5 nm nanocomposite, compensating for the concomitant weakness accompanying the change to a coherent interface.

8. Conclusions

In this work, using a combination of nanomechanical testing and 3D crystal plasticity finite element (CPFE) modeling, we investigate the strengthening mechanisms of pseudomorphic BCC Mg/Nb nanocomposites. We focused on a set of nanocomposites, which were synthesized via physical vapor deposition (PVD) to have one of three layer thickness composite, 35/65, 7/7 and 5.5/5.5 nm. The mechanical response in compression applied either normal, parallel or 45° to the Mg/Nb interface planes are carried out via micropillar compression testing to assess plastic anisotropy. Among the suite of tests, the response of the intermediate layer thickness 7/7 nm nanocomposites and the large strain response of the 5.5/5.5 nm composite tested 45° to the interface layers are new. Altogether, they made a complete set of composites differing in crystal structure of the Mg phase, Mg/Nb interface type, and texture. To identify the individual roles of the interface and pseudomorphic phase transition to the deformation behavior, we construct a 3D CPFE model of the two-phase polycrystalline laminate and incorporate into it, an extended confined layer slip model, called dual-mode CLS. The model differs from the conventional version by incorporating the interaction not only between the gliding dislocation and the bimetal interfaces, but also interactions with the grain boundaries. In dual-mode CLS, dislocation glide is separated into glide parallel to the interfaces, in which dislocations directly interact with the grain boundaries and not the interfaces, and glide non-parallel to the interfaces, which directly interact with the biphase interfaces. The first mode does not lead to a layer size effect on dislocation motion, is affected by the grain boundary energy, and is relatively easier, while the second mode does have a layer size effect, is affected by the biphase energy, and is relatively harder. In the experiment, we find that the flow stress and plastic anisotropy of the nano-layered composite scale inversely with the layer thickness. The CPFE model with the dual CLS law agrees well these mechanical responses during the compression in three directions and in all three composites using one set of material parameters. Analysis of the model predictions and associated parameters identify that the higher strength for the BCC/BCC Mg/Nb composite is contributed by the initial resistance, finer thickness and primarily due to the BCC Mg phase itself. The results also show that the incoherent HCP/BCC MgNb interface provides much more resistance to dislocation propagation than the BCC/BCC coherent interface. The present model does not include a backstress term from strain gradient theory, since the nanolayers are too fine for a pile up to develop and the current model is aimed at capturing the layer size effect on strength. Nevertheless, accounting for backstress due to strain gradient would further improve the model. Such developments will be part of future works.

CRediT authorship contribution statement

Jiaxiang Wang: Conceptualization, Data curation, Formal analysis, Investigation, Writing - original draft. **Marko Knezevic:** Methodology, Software, Writing – review & editing, Funding acquisition. **Manish Jain:** Formal analysis, Resources. **Siddhartha Pathak:** Writing – review & editing, Formal analysis, Resources. **Irene J. Beyerlein:** Conceptualization, Writing – review & editing, Supervision, Funding acquisition, Resources.

Declaration of Competing Interest

The authors declare that they have no known competing financial interests or personal relationships that could have appeared to influence the work reported in this paper.

Acknowledgments

The authors gratefully acknowledge support from the U.S. National Science Foundation (NSF) under grant no. CMMI-1728224 (UCSB) and CMMI-1727495 (UNH). SP acknowledges equipment funding from NSF MRI #1726897 and DOE DE-NE0008739 for this work. This work was performed, in part, at the Center for Integrated Nanotechnologies, an Office of Science User Facility operated for the U.S. Department of Energy (DOE) Office of Science. Los Alamos National Laboratory, an affirmative action equal opportunity employer, is managed by Triad National Security, LLC, for the National Nuclear Security Administration of the U.S. Department of Energy under contract 89233218CNA000001.

Appendix

Figs. A1–A3

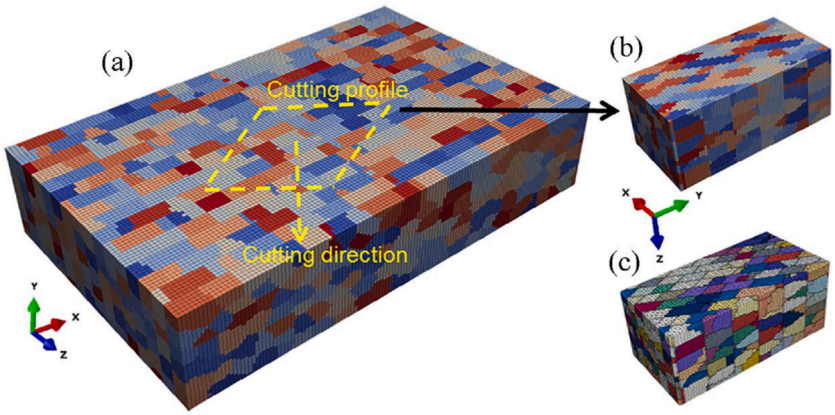

Fig. A1. Schematic of the developed procedure for 45° finite element model generation. (a) Large scale voxel-based model that contains large number of layers used for cutting, (b) 45° voxel-based model obtained as a result of cutting, (c) corresponding 45°FE model. Reprinted with permission from Su et al. (2020).

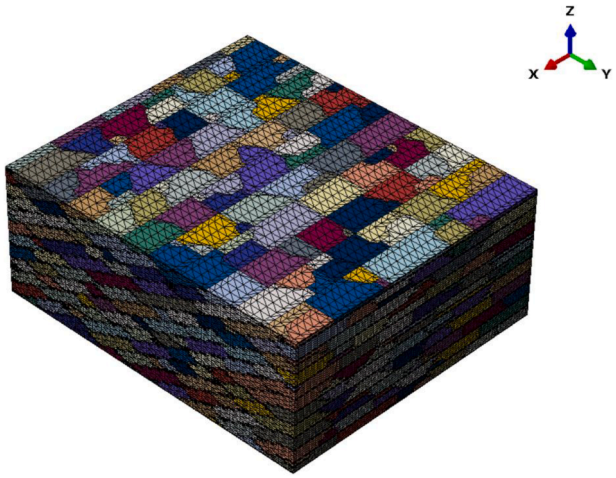

Fig. A2. Finite element meshes used in the crystal plasticity calculations for the 5.5/5.5 nm composite in 45°compression.

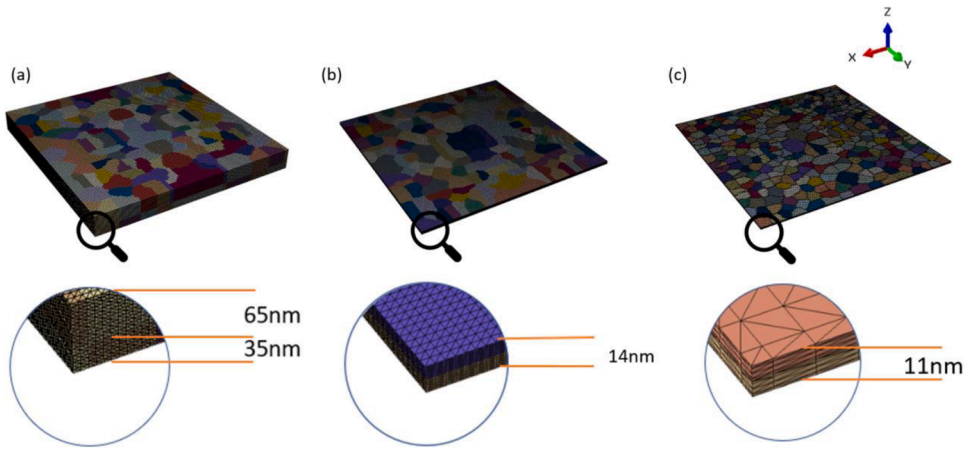

Fig. A3. Finite element meshes used in the crystal plasticity calculations for the (a) 35/65 nm (b) 7/7 nm (c) 5.5/5.5 nm composites. The zoom in view in the insets help to show the mesh used within the individual layers.

References

Al–Fadhalah, K., Tomé, C.N., Beaudoin, A.J., Robertson, I.M., Hirth, J.P., Misra, A., 2005. Modeling texture evolution during rolling of a Cu–Nb multilayered system. Philos. Mag. 85, 1419–1440.

Anderson, P.M., Foecke, T., Hazzledine, P.M., 1999. Dislocation-based deformation mechanisms in metallic nanolaminates. Mrs. Bull. 24, 27–33.

Ardeljan, M., Beyerlein, I.J., Knezevic, M., 2014. A dislocation density based crystal plasticity finite element model: application to a two-phase polycrystalline HCP/BCC composites. J. Mech. Phys. Solids 66, 16–31.

Ardeljan, M., Beyerlein, I.J., McWilliams, B.A., Knezevic, M., 2016. Strain rate and temperature sensitive multi-level crystal plasticity model for large plastic deformation behavior: application to AZ31 magnesium alloy. Int. J. Plast. 83, 90–109.

Ardeljan, M., Knezevic, M., 2018. Explicit modeling of double twinning in AZ31 using crystal plasticity finite elements for predicting the mechanical fields for twin variant selection and fracture analyses. Acta Mater 157, 339–354.

Ardeljan, M., Knezevic, M., Jain, M., Pathak, S., Kumar, A., Li, N., Mara, N.A., Baldwin, J.K., Beyerlein, I.J., 2018. Room temperature deformation mechanisms of Mg/Nb nanolayered composites. J. Mater. Res. 33, 1311–1332.

Ardeljan, M., Knezevic, M., Nizolek, T., Beyerlein, I.J., Mara, N.A., Pollock, T.M., 2015. A study of microstructure-driven strain localizations in two-phase polycrystalline HCP/BCC composites using a multi-scale model. Int. J. Plast. 74, 35–57.

Arul Kumar, M., Beyerlein, I.J., Tomé, C.N., 2017. A measure of plastic anisotropy for hexagonal close packed metals: application to alloying effects on the formability of Mg. J. Alloy Compd. 695, 1488–1497.

Asaro, R.J., Needleman, A., 1985. Texture development and strain hardening in rate dependent polycrystals. Acta Metall. et Mater. 33, 923–953.

Barrett, T.J., Savage, D.J., Ardeljan, M., Knezevic, M., 2018. An automated procedure for geometry creation and finite element mesh generation: application to explicit grain structure models and machining distortion. Comp. Mater Sci. 141, 269–281.

Bathe, K.-J., 1996. Finite Element Procedures. Prentice Hall, Englewood Cliffs, N.J.

Beyerlein, I.J., Demkowicz, M.J., Misra, A., Uberuaga, B.P., 2015. Defect-interface interactions. Prog. Mater Sci. 74, 125–210.

Bolef, D., 1961. Elastic constants of single crystals of the BCC transition elements V, Nb, and Ta. J. Appl .Phys. 32, 100–105.

Bong, H.J., Hu, X., Sun, X., Ren, Y., 2019. Mechanism-based constitutive modeling of ZEK100 magnesium alloy with crystal plasticity and in-situ HEXRD experiment. Int. J. Plast. 113, 35–51.

Bronkhorst, C., Cerreta, E., Xue, Q., Maudlin, P., Mason, T., Gray, G., 2006. An experimental and numerical study of the localization behavior of tantalum and stainless steel. Int. J. Plast. 22, 1304–1335.

Bronkhorst, C.A., Kalidindi, S.R., Anand, L., 1992. Polycrystalline plasticity and the evolution of crystallographic texture in FCC metals. Philosoph. Trans. R. Soc. Lond. Ser. A-Math. Phys. Eng. Sci. 341, 443–477.

Cao, Z.H., Cai, Y.P., Sun, C., Ma, Y.J., Wei, M.Z., Li, Q., Lu, H.M., Wang, H., Zhang, X., Meng, X.K., 2019. Tailoring strength and plasticity of Ag/Nb nanolaminates via intrinsic microstructure and extrinsic dimension. Int. J. Plast. 113, 145–157.

Chen, H.H., Zhao, Y.F., Zhang, J.Y., Wang, Y.Q., Li, G.Y., Wu, K., Liu, G., Sun, J., 2020a. He-ion irradiation effects on the microstructure stability and size-dependent mechanical behavior of high entropy alloy/Cu nanotwinned nanolaminates. Int. J. Plast. 133.

Chen, T.J., Yuan, R., Beyerlein, I.J., Zhou, C.Z., 2020b. Predicting the size scaling in strength of nanolayered materials by a discrete slip crystal plasticity model. Int. J. Plast. 124, 247–260.

Chen, Y., Gong, M.Y., Shao, S., Mara, N.A., Wang, J., 2019. Interface facilitated reorientation of Mg nanolayers in Mg-Nb nanolaminates. JOM-Us 71, 1215–1220.

Cho, H., Bronkhorst, C.A., Mourad, H.M., Mayeur, J.R., Luscher, D.J., 2018. Anomalous plasticity of body-centered-cubic crystals with non-Schmid effect. Int. J. Solids Struct. 139, 138–149.

Clemens, B.M., Kung, H., Barnett, S.A., 1999. Structure and strength of multilayers. Mrs. Bull. 24, 20–26.

Frank, F.C., Vandermerwe, J.H., 1949. One-dimensional dislocations .1. Static Theory. Proc. R Soc. Lond. Ser. A 198, 205–216.

Ham, B., Zhang, X., 2011. High strength Mg/Nb nanolayer composites. Mater. Sci. Eng. A 528, 2028–2033.

Han, W.Z., Misra, A., Mara, N.A., Germann, T.C., Baldwin, J.K., Shimada, T., Luo, S.N., 2011. Role of interfaces in shock-induced plasticity in Cu/Nb nanolaminates. Philos Mag. 91, 4172–4185.

Hansen, B.L., Beyerlein, I.J., Bronkhorst, C.A., Cerreta, E.K., Dennis-Koller, D., 2013. A dislocation-based multi-rate single crystal plasticity model. Int. J. Plast. 44, 129–146.

Hoagland, R.G., Kurtz, R.J., Henager, C.H., 2004. Slip resistance of interfaces and the strength of metallic multilayer composites. Scripta Mater 50, 775–779.

Hutchinson, J.W., 1976. Bounds and self-consistent estimates for creep of polycrystalline materials. Proc. R Soc. Lond. A Math. Phys. Sci. 348, 101–126.

Jahedi, M., Ardeljan, M., Beyerlein, I.J., Paydar, M.H., Knezevic, M., 2015. Enhancement of orientation gradients during simple shear deformation by application of simple compression. J. Appl. Phys. 117, 214309.

Jain, M., TK, A., Yaddanapudi, K., Bahr, J., Knezevic, M., 2021. Simultaneous high strength and mechanical stability with sub-10nm layered bcc Mg/Nb nanolaminates".

Jain, M., Velisavljevic, N., Baldwin, J.K., Knezevic, M., Mara, N.A., Beyerlein, I.J., Pathak, S., 2019. Structure and properties of pseudomorphically transformed BCC Mg in Mg/Nb multilayered nanolaminates studied using synchrotron X-ray diffraction. J. Appl. Phys. 126.

Jesser, W.A., 1969. A Theory of Pseudomorphism in Thin Films. Mater Sci. Eng. 4, 279.

Kabirian, F., Khan, A.S., Gnäupel-Herlod, T., 2015. Visco-plastic modeling of mechanical responses and texture evolution in extruded AZ31 magnesium alloy for various loading conditions. Int. J. Plast. 68, 1–20.

Kalidindi, S.R., 1998. Incorporation of deformation twinning in crystal plasticity models. J. Mech. Phys. Solids 46, 267–271.

Kalidindi, S.R., Bronkhorst, C.A., Anand, L., 1992. Crystallographic texture evolution in bulk deformation processing of FCC metals. J. Mech. Phys. Solids 40, 537–569.

Kalidindi, S.R., Duvvuru, H.K., Knezevic, M., 2006. Spectral calibration of crystal plasticity models. Acta Mater 54, 1795–1804.

Knezevic, M., Beyerlein, I.J., 2018. Multiscale modeling of microstructure-property relationships of polycrystalline metals during thermo-mechanical deformation. Adv. Eng. Mater. 20, 1700956.

Knezevic, M., Drach, B., Ardeljan, M., Beyerlein, I.J., 2014. Three dimensional predictions of grain scale plasticity and grain boundaries using crystal plasticity finite element models. Comput. Methods Appl. Mech. Eng. 277, 239–259.

Kumar, A., Beyerlein, I.J., Wang, J., 2014. First-principles study of the structure of Mg/Nb multilayers. Appl. Phys. Lett. 105.

Kumar, M.A., Beyerlein, I.J., Lebensohn, R.A., Tome, C.N., 2017a. Role of alloying elements on twin growth and twin transmission in magnesium alloys. Mat. Sci. Eng. A Struct. 706, 295–303.

Kumar, M.A., Beyerlein, I.J., Tome, C.N., 2017b. A measure of plastic anisotropy for hexagonal close packed metals: application to alloying effects on the formability of Mg. J. Alloy Compd. 695, 1488–1497.

Lebensohn, R.A., Tomé, C.N., 1993. A self-consistent anisotropic approach for the simulation of plastic deformation and texture development of polycrystals: application to zirconium alloys. Acta Metall. et Mater. 41, 2611–2624.

Lentz, M., Risse, M., Schaefer, N., Reimers, W., Beyerlein, I., 2016. Strength and ductility with $\{10\bar{1}1\}$—$\{10\bar{1}2\}$ double twinning in a magnesium alloy. Nat. Commun. 7, 1–7.

Liu, G.S., Xie, D.Y., Wang, S.J., Misra, A., Wang, J., 2019. Mesoscale crystal plasticity modeling of nanoscale Al-Al2Cu eutectic alloy. Int. J. Plast. 121, 134–152.

Mara, N., Beyerlein, I., 2014. Review: effect of bimetal interface structure on the mechanical behavior of Cu–Nb FCC–BCC nanolayered composites. J. Mater. Sci. 49, 6497–6516.

Mara, N.A., Beyerlein, I.J., 2015. Interface-dominant multilayers fabricated by severe plastic deformation: stability under extreme conditions. Curr. Opin. Solid St M 19, 265–276.

Mara, N.A., Bhattacharyya, D., Hoagland, R.G., Misra, A., 2008. Tensile behavior of 40nm Cu/Nb nanoscale multilayers. Scripta Mater 58, 874–877.

Mastorakos, I.N., Zbib, H.M., Bahr, D.F., 2009. Deformation mechanisms and strength in nanoscale multilayer metallic composites with coherent and incoherent interfaces. Appl. Phys. Lett. 94.
Miller, V.M., Berman, T.D., Beyerlein, I.J., Jones, J.W., Pollock, T.M., 2016. Prediction of the plastic anisotropy of magnesium alloys with synthetic textures and implications for the effect of texture on formability. Mat. Sci. Eng. A Struct. 675, 345–360.
Misra, A., Hirth, J., Hoagland, R., 2005. Length-scale-dependent deformation mechanisms in incoherent metallic multilayered composites. Acta Mater 53, 4817–4824.
Misra, A., Hoagland, R., Kung‡, H., 2004. Thermal stability of self-supported nanolayered Cu/Nb films. Philos. Mag. 84, 1021–1028.
Misra, A., Hoagland, R.G., 2005. Effects of elevated temperature annealing on the structure and hardness of copper/niobium nanolayered films. J. Mater. Res. 20, 2046–2054.
Misra, A., Verdier, M., Kung, H., Embury, J.D., Hirth, J.P., 1999. Deformation mechanism maps for polycrystalline metallic multilayers (vol 41, pg 973, 1999). Scripta Mater 42, 219. -219.
Nix, W.D., 1989. Mechanical-properties of thin-films. Metall. Trans. A 20, 2217–2245.
Nizolek, T., Beyerlein, I.J., Mara, N.A., Avallone, J.T., Pollock, T.M., 2016. Tensile behavior and flow stress anisotropy of accumulative roll bonded Cu-Nb nanolaminates. Appl. Phys. Lett. 108, 051903.
Pan, H.C., Ren, Y.P., Fu, H., Zhao, H., Wang, L.Q., Meng, X.Y., Qin, G.W., 2016. Recent developments in rare-earth free wrought magnesium alloys having high strength: a review. J. Alloy Compd. 663, 321–331.
Pathak, S., Li, N., Maeder, X., Hoagland, R.G., Baldwin, J.K., Michler, J., Misra, A., Wang, J., Mara, N.A., 2015. On the origins of hardness of Cu-TiN nanolayered composites. Scripta Mater 109, 48–51.
Pathak, S., Velisavljevic, N., Baldwin, J.K., Jain, M., Zheng, S., Mara, N.A., Beyerlein, I.J., 2017. Strong, ductile, and thermally Stable BCC-Mg Nanolaminates. Sci. Rep. 7, 8264.
Risse, M., Lentz, M., Fahrenson, C., Reimers, W., Knezevic, M., Beyerlein, I.J., 2017. Elevated Temperature effects on the plastic anisotropy of an extruded Mg-4 Wt Pct Li alloy: experiments and polycrystal modeling. Metall. Mater. Trans. A 48, 446–458.
Roters, F., Eisenlohr, P., Hantcherli, L., Tjahjanto, D.D., Bieler, T.R., Raabe, D., 2010. Overview of constitutive laws, kinematics, homogenization and multiscale methods in crystal plasticity finite-element modeling: theory, experiments, applications. Acta Mater. 58, 1152–1211.
Sandlöbes, S., Zaefferer, S., Schestakow, I., Yi, S., Gonzalez-Martinez, R., 2011. On the role of non-basal deformation mechanisms for the ductility of Mg and Mg–Y alloys. Acta Mater 59, 429–439.
Savage, D.J., Beyerlein, I.J., Mara, N.A., Vogel, S.C., McCabe, R.J., Knezevic, M., 2020. Microstructure and texture evolution in Mg/Nb layered materials made by accumulative roll bonding. Int. J. Plast. 125, 1–26.
Slutsky, L.J., Garland, C.W., 1957. Elastic Constants of Magnesium from 4.2K to 300K. Phys. Rev. 107, 972–976.
Snel, J., Monclus, M.A., Castillo-Rodriguez, M., Mara, N., Beyerlein, I.J., Llorca, J., Molina-Aldareguia, J.M., 2017. Deformation mechanism map of Cu/Nb nanoscale metallic multilayers as a function of temperature and layer thickness. JOM-Us 69, 2214–2226.
Su, Y.Q., Ardeljan, M., Knezevic, M., Jain, M., Pathak, S., Beyerlein, I.J., 2020. Elastic constants of pure body-centered cubic Mg in nanolaminates. Comp. Mater Sci. 174.
Subedi, S., Beyerlein, I.J., Lesar, R., Rollett, A.D., 2018. Strength of nanoscale metallic multilayers. Scripta Mater 145, 132–136.
Wang, J., Zecevic, M., Knezevic, M., Beyerlein, I.J., 2020. Polycrystal plasticity modeling for load reversals in commercially pure titanium. Int. J. Plast. 125, 294–313.
Wang, M., Beyerlein, I.J., Zhang, J., Han, W.Z., 2018. Defect-interface interactions in irradiated Cu/Ag nanocomposites. Acta Mater 160, 211–223.
Weinberger, C.R., Battaile, C.C., Buchheit, T.E., Holm, E.A., 2012. Incorporating atomistic data of lattice friction into BCC crystal plasticity models. Int. J. Plast. 37, 16–30.
Weinberger, C.R., Tucker, G.J., Foiles, S.M., 2013. Peierls potential of screw dislocations in BCC transition metals: predictions from density functional theory. Phys. Rev. B 87.
Yang, W.F., Beyerlein, I.J., Jin, Q.Q., Ge, H.L., Xiong, T., Yang, L.X., Pang, J.C., Zhou, Y.T., Shao, X.H., Zhang, B., Zheng, S.J., Ma, X.L., 2019. Strength and ductility of bulk Cu/Nb nanolaminates exposed to extremely high temperatures. Scripta Mater 166, 73–77.
Zbib, H.M., Overman, C.T., Akasheh, F., Bahr, D., 2011. Analysis of plastic deformation in nanoscale metallic multilayers with coherent and incoherent interfaces. Int. J. Plast. 27, 1618–1639.
Zecevic, M., McCabe, R.J., Knezevic, M., 2015a. A new implementation of the spectral crystal plasticity framework in implicit finite elements. Mech. Mater. 84, 114–126.
Zecevic, M., McCabe, R.J., Knezevic, M., 2015b. Spectral database solutions to elasto-viscoplasticity within finite elements: application to a cobalt-based FCC superalloy. Int. J. Plast. 70, 151–165.
Zeng, Z.R., Stanford, N., Davies, C.H.J., Nie, J.F., Birbilis, N., 2019. Magnesium extrusion alloys: a review of developments and prospects. Int. Mater Rev. 64, 27–62.
Zhang, H.J., Jerusalem, A., Salvati, E., Papadaki, C., Fong, K.S., Song, X., Korsunsky, A.M., 2019. Multi-scale mechanisms of twinning-detwinning in magnesium alloy AZ31B simulated by crystal plasticity modeling and validated via in situ synchrotron XRD and in situ SEM-EBSD. Int J. Plast. 119, 43–56.
Zhang, J.Y., Wu, K., Zhang, L.Y., Wang, Y.Q., Liu, G., Sun, J., 2017. Unraveling the correlation between Hall-Petch slope and peak hardness in metallic nanolaminates. Int J. Plast. 96, 120–134.
Zhao, L., Guo, Q., Li, Z.Q., Xiong, D.B., Osovski, S., Su, Y.S., Zhang, D., 2019. Strengthening and deformation mechanisms in nanolaminated graphene-Al composite micro-pillars affected by graphene in-plane sizes. Int. J. Plast. 116, 265–279.